

Received 5 November 2024, accepted 20 November 2024, date of publication 27 November 2024, date of current version 9 December 2024.

Digital Object Identifier 10.1109/ACCESS.2024.3507370



Hyperspectral In-Situ Monitoring for Deep Learning-Based Anomaly Classification in Metal Additive Manufacturing

CHARLES SNYERS^[D], JULIEN ERTVELDT¹, KYRIAKOS EFTHYMIADIS², AND JAN HELSEN¹
Department of Mechanical Engineering, Vrije Universiteit Brussel, 1050 Brussels, Belgium

²Department of Computer Science, Vrije Universiteit Brussel, 1050 Brussels, Belgium

Corresponding author: Charles Snyers (charles.snyers@vub.be)

This work was supported by the Strategisch Basis Onderzoek (SBO) Robustify grant of the Fonds Wetenschappelijk Onderzoek (FWO).

ABSTRACT Metal Additive Manufacturing processes such as Directed Energy Deposition (DED) require process monitoring to ensure the highest part quality. Detecting and avoiding material defects to meet high material requirements remains a challenge due to the complexity of the process. To address this challenge, this study presents a novel approach that combines hyperspectral imaging with convolutional neural networks to classify process anomalies. Hyperspectral in-situ monitoring captures the light emitted from the melt pool over the 2 spatial axis, but also over the spectral axis. The resulting hypercube image contains a lot of information over the thermal state of the melt pool but is very high-dimensional, which is not a problem for Convolutional Neural Networks. The proposed classification model reaches an accuracy in excess of 94% over the validation set. The classification mechanism of the proposed model is investigated thanks to the Guided GradCAM visualization method and links with the melt pool temperature distribution are formulated. The inference speed of the optimized model is measured and shown to be compatible with realtime applications. This study is a stepping stone towards smart control of the DED process based on the identified thermal state of the melt pool, with the goal of improving the part quality.

INDEX TERMS Directed energy deposition, convolutional neural network, anomaly classification, In-situ monitoring, hyperspectral imaging.

I. INTRODUCTION

A. DIRECTED ENERGY DEPOSITION AND IN-SITU MONITORING

Laser-based Directed Energy Deposition (DED) is a complex manufacturing process to 3D print metal parts. A powerful laser heats and melts a metal workpiece, and fine metallic powder is blown into the melt pool through a nozzle. As the nozzle and the laser move, the melted metal solidifies, building up layers to create the final part [1]. This process gives a high freedom of design and enables the production of complex shapes, for example rocket nozzles with integrated cooling channels or rocket combustion chambers [2], [3]. As in other metal Additive Manufacturing (AM) techniques, there is a complex interplay of several simultaneous physical

The associate editor coordinating the review of this manuscript and approving it for publication was Agustin Leobardo Herrera-May.

phenomena happening on the melt pool scale: radiative heat exchange between the laser and metal workpiece, liquid flow in the melt pool, phase changes, powder and gas dynamics, etc. [1], [4], [5], [6]. On the part scale, the intricate features of the printed designs and the layer-by-layer construction create a complex thermal history. As a result, the several kind of defects can be created during the process, i.e. flaws that do not meet the application requirements. Given the difference in scale between the melt pool and the part geometry, simulating both the melt pool dynamics and the thermal history together to cover as many sources of defects as possible, is currently a challenge [7], [8].

To capture the full complexity of the DED process and avoid defects, there has been a lot of effort to monitor in-situ the melt pool infrared (IR) signature [9], [10], [11]. IR melt pool measurements allow the estimation of the temperature distribution in and around the melt pool by using Planck's law



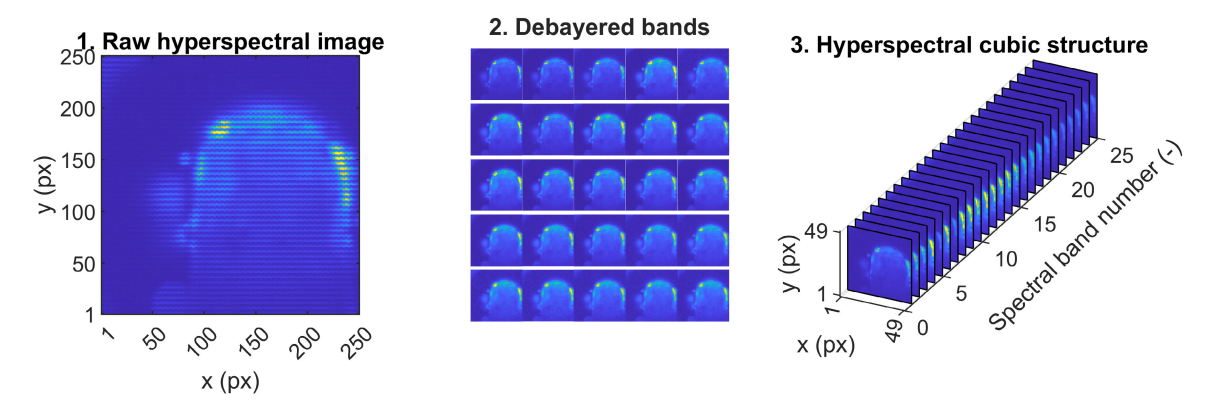


FIGURE 1. Visualization of the steps to debayer a raw hyperspectral image and obtain a hyperspectral data cube. Each slice of the cubic structure in the spectral axis can be seen as a 2D image at one spectral band. The resulting cubic structure is high-dimensional.

and an estimation of the material emissivity. The temperature signal can then be used for condition monitoring or closed loop control [12], [13]. However, estimating temperature from IR data requires a model the emissivity, which is another challenge on its own since in all generality emissivity is a function of wavelength, temperature, phase, surface roughness and material composition [10]. The approximation of emissivity is therefore a limiting factor for the use of the temperature signal. In this regard, hyperspectral IR cameras are superior to monospectral IR cameras because they measure the light emitted by the melt pool at several wavelength bands. Hyperspectral data can be used to estimate the relationship between emissivity and wavelength. But there is still a debate on which temperature estimation method yields the most accurate results [14]. Moreover, hyperspectral images are essentially cubic structures of data: they contain information organised along two spatial dimensions, x and y, and one spectral dimension, λ . The high-dimensionality of those images is therefore a burden to process, especially for real-time applications. Fig. 1 shows the steps to obtain a hyperspectral data cube with a discrete amount of spectral bands. The data along each spectral band of the cube can be seen as a conventional 2D image, but the cube is actually captured as a whole during the exposure time of the camera.

Other in-situ monitoring techniques are being used and studied for DED, such as acoustic emission and radiography. The advantages and limitations of those techniques have been discussed and compared in detail in several review articles [15], [16], [17].

To summarize, monitoring the melt pool IR signature gives a lot of information on the state of the process, but analysing high-dimensional hyperspectral IR data with temperature estimation methods is challenging and time-consuming.

B. DATA-DRIVEN ALGORITHMS FOR ANOMALY CLASSIFICATION

To overcome the limitations of temperature estimation algorithms and physics-based models, a direct correlation between the presence of defects and the melt pool IR signature is desirable. Data-driven algorithms are well

adapted to interpret raw experimental data without making inherent hypothesis on the melt pool dynamics or material properties.

Shallow Learning methods have been applied successfully to features extracted from melt pool IR images [24], [27], but the curse of dimensionality prevents them from using raw high-dimensional images as direct inputs [28]. Modern Deep Learning (DL) techniques such as Convolutional Neural Networks (CNN) allow the classification such high-dimensional image datasets [29], [30]. Those algorithms have more trainable parameters than shallow methods and therefore require larger datasets to generalize well. They also enable fast predictions despite having many parameters thanks to parallel computing on Graphical Processing Units (GPUs).

Modern CNN models have been historically developed for the classification of natural RGB images, but they have also recently been applied to melt pool IR signatures. Table 1 lists past studies that have used data-driven models to link in-situ melt pool images to the presence of defects or anomalies in three laser-based metal processes. From this body of work, it is clear that in-situ melt pool images can be successfully correlated with the presence of defects or anomalies. We can see that many authors achieved to build binary classification models with accuracies above 90% regardless of the type of melt pool image used [18], [20], [23], [31]. Researchers that attempted multiclass classification with monochrome melt pool images in DED and LPBF achieved a lower accuracy, between 80 and 90% [22], [24]. Only Cai et al. achieved an accuracy over 90% for multiclass classification of monochrome melt pool images in laser welding [26].

From the literature, it seems clear that spectral IR measurements offer an advantage over monochrome or monoband measurements. Knaak et al. [25] combined data from one Near-Infrared (NIR) camera and one Middle-Wavelength-Infrared (MWIR) camera to predict the presence of defects in laser welding. It was demonstrated in this work that the combination of NIR and MWIR ranges resulted in a higher classification accuracy than either of the two ranges alone. Gerdes et al. [32] used melt pool images captured with a hyperspectral camera sensitive to 25 different bands in the



Ref.	Process	Algorithm	Model input	Model prediction	Ground truth	Dataset images	Accuracy on test set
[18]	DED	CNN	MP temp. field	Binary porosity detection	CT	1564	96 %
[19]		CNN	Visible-light MP image	Binary porosity detection	CT and cuts	14 632	91.2 %
[20]		LSTM&CNN	MP temp. field & LWIR image	Binary porosity detection	CT	840	98.9 %
[21]		ConvLSTM	Visible-light MP image	Binary anomaly detection	Unlabelled	12 158	NA
[22]		CNN	IR MP image	1 of 4 process conditions	Process parameter	211	≈ 80 %
[23]	LPBF	CNN	SWIR MP image	Binary porosity detection	CT	836 426	96 %
[24]		SIFT&BoW	Visible-light MP image	1 of 5 defect classes	Process parameters	24 385	85.1%
[25] [26]	Laser welding	CNN CNN	NIR & MWIR MP image NIR MP image	1 of 6 defect classes 1 of 4 penetration classes	Expert identification Expert identification	14 530 720	97.8 % 98.5 %

TABLE 1. Literature review of past work on anomaly classification of melt pool (MP) images and features in DED, LPBF and laser welding. A gap in literature exists regarding the use of raw hyperspectral data with a CNN to predict anomalies in DED.

NIR range to predict the surface roughness and showed that hyperspectral data provided crucial information about the Laser-baser Powder Bed Fusion (LPBF) process. A simple CNN was applied to the very high-dimensional data and could successfully correlate it with roughness despite the additional channels compared to a natural image. To the best of the authors' knowledge, DED hyperspectral data have not yet been used in conjunction with CNNs to detect defects.

To classify labelled samples, a source of ground truth must be chosen to detect defects. In some studies, a exsitu sensor is used: Computed Tomography (CT) to locate porosities [18], [19], [20], [23] or a confocal microscope to measure roughness [32]. And in others, images are labelled manually by experts [25], [26]. Detecting defects in such a way is usually accurate but either expensive or time-consuming with regard to the amound of data required to train CNNs. In this regard, Abranovic et al. took an unsupervised learning approach to avoid the ground truth problem, but with a simpler binary anomaly detection model.

Controlling process parameters is straightforward and the link between DED process parameters, defects and unfavourable mechanical properties is well described in literature for simple geometries [33], [34]. Therefore, this paper uses variation of process parameters to create several types of thermal conditions similar to those of known defects [35]. In this work, the thermal conditions that deviate from a chosen baseline, are called thermal anomalies.

This work is structured as follows: section II describes the experimental set-up, the dataset and the model structure, and section III analyses and discusses the model performance.

The novel aspects of this study are:

- An efficient data labelling method for several classes of anomalies that allows the creation of a large dataset of in-situ melt pool images.
- The development of an anomaly classification model based on high-dimensional hyperspectral melt pool images and a CNN architecture.
- The investigation of the classification model's potential for real time applications.
- The use of saliency methods to investigate the classification mechanism over the spatial and spectral axes.

II. MATERIAL AND METHODS

A. DED MACHINE AND HYPERSPECTRAL MONITORING

In this section, the experimental set-up, process parameters and the samples are described.

The experimental setup that is used to print samples and produce the raw in situ monitoring data is the MiCLAD research platform, a DED machine designed and built at the Vrije Universiteit Brussel (VUB) [37]. It is equipped with several in-situ sensors and cameras. The main hardware parts of this machine are listed in table 2. A view of the laser processing head and build plate is shown in fig. 2.



FIGURE 2. MiCLAD research platform: view of the laser processing head and build plate. The hyperspectral camera is attached to the top of the laser processing head (outside of the image).

The DED process creates a metal melt pool by locally heating the workpiece with a laser. The light emitted by the melt pool gives information on the melt pool shape and state, as the emitted spectral radiance depends on the melt pool temperature following Planck's law [38]. It has been



TABLE 2. Hardware, printing and acquisition parameters used to produce the experimental data.

Hardware			
Laser	SPI redPOWER® QUBE 2kW, 1064nm, 2.55mm fibre, flat-top		
Processing head	Precitec YC52		
Nozzle	Harald Dickler HighNo 4.0		
Printing parameters			
Laser power	600 W		
Baseline scanning speed	900 mm/min		
Powder	316L 45–105 μm		
Powder flow rate	3.5 g/min		
Layer thickness	0.2 mm		
Hyperspectral camera			
Model	3D-One Avior AX-M25NIR		
Mosaic filter layout	5x5		
Wavelength peaks of the 25 bands	690, 703, 714, 730, 731, 742, 742,		
	755, 771, 784, 794, 810, 820, 833,		
	848, 858, 870, 884, 895, 904, 918,		
	926, 936, 945, and 954 nm		
Resolution	250 x 250 px		
Exposure	200 us		
Framerate	500 Hz		

shown in literature that the typical DED melt pool has an elliptical shape with a thin, high temperature front edge and an elongated, lower temperature tail edge [2], [5], [39].

The MiCLAD machine is equipped with the hyperspectral 3D-One Avior AX-M25NIR camera, installed coaxially to the nozzle. This camera was selected and used due to its availability during the course of the study. It uses a hyperspectral sensor that is active in the near infrared region (NIR) to capture the melt pool spectral signature. A Fabry-Perot filter is deposited on each pixel in a 5×5 mosaic pattern. Thanks to the Fabry-Perot filter, each pixel of the 5×5 mosaic pattern is sensitive to a different band, which allows the camera to observe the 25 bands at the same exposure time. The raw image recorded by the camera has a resolution of 250×250 pixels. This 2D image can be reconstructed into a 3D structure, a $25 \times 49 \times 49$ cube (see fig. 1) by first grouping together all pixels that are sensitive to the same band and arranging the spectral bands by increasing order of wavelength. This operation is known as debayering. The difference in pixel count between the raw image and the cubic structure is due to a misalignment between the edges of the macropixels located on the border and the edges of the raw 250×250 hyperspectral image. Those macropixels located at the edge of the region-of-interest captured by the camera are incomplete because a portion of their 5×5 pixels are located outside of the region-of-interest. Those macropixels therefore cannot be debayered and are discarded during the debayering step. As a result there are less pixels in the cubic structure. The main characteristics and the peaks of the 25 bands of the hyperspectral camera are listed in table 2. The MiCLAD machine has also the capability to monitor and record its position every time an image is recorded by the hyperspectral

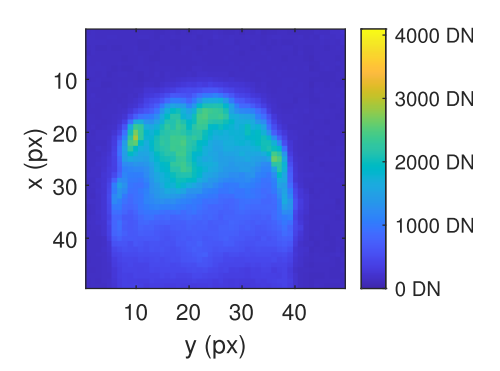


FIGURE 3. Single NIR band of a DED melt pool, extracted from a hyperspectral cube (at the peak wavelength $\lambda = 784\,nm$) captured on the MiCLAD machine with the 3D-One Avior AX-M25NIR. This image shows the typical front edge of the melt pool.

camera. Therefore, each image is associated with the position of the nozzle when the image was recorded.

Fig. 3 shows a single band image of a typical DED melt pool, extracted from a hyperspectral cubic structure. This image showcases the front edge of the melt pool. The shape and temperature of the melt pool front and tail edges depend on the laser power and scanning speed, among other process parameters.

The experiment consisted in printing 4 thin wall samples (samples 587, 588, 589 and 590) of 80 mm long and 20 mm high with 316L steel powder. These samples were made by depositing a track back and forth, incrementing the Z position by a fixed value after every pass. The parameters used to print the samples are in table 2. The nozzle scanning speed was varied during the print, as explained in the following section.

B. THERMAL ANOMALIES AND LABELLING METHOD

In this section, the method used to produce thermal anomalies and label the dataset images accordingly, is described [35].

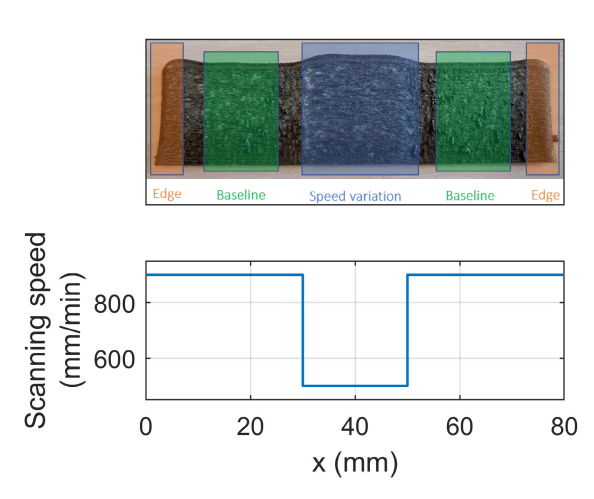


FIGURE 4. Scheme illustrating the zones linked to melt pool classes and the associated local scanning speed (sample 590).

As the laser and the associated heat flux move during printing, the melt pool also moves and is affected by local geometry conditions, the laser scanning path and the thermal



history of the part. This can cause the melt pool shape and temperature distribution to vary and it can ultimately lead to undesired melt pools regimes such as keyhole, lack-of-fusion or the formation of gas porosities [2], [5].

The energy density E_d is a simplified approach to represent the energy deposition into the build plate and the part, that has been correlated to melt pool thermal conditions, mechanical properties and the presence of defects in DED [2], [5].

$$E_d = \frac{P}{v \cdot d} \tag{1}$$

where P is the laser power, v is the scanning speed and d is the laser diameter.

In order to produce representative data of undesired melt pool behaviours, it was decided to vary the scanning speed of the nozzle to change the deposited energy density E_d and induce significant differences in the thermal conditions of the process. Each thin wall sample was subdivided in several zones, depending on the local process parameters and thermal conditions (see fig. 4):

- **Speed variation zone:** The central zone of the thin wall is where the scanning speed deviate from the baseline. This is one way to create a thermal anomaly. 4 different speeds were considered for this zone, one for each sample, and each speed was associated with a anomaly class (see table 3). The melt pool behaviour in these zones is labelled depending on the scanning speed deviation (see table 3).
- Baseline zones: In the two zones to left and the right
 of the central zone, the scanning speed is kept at the
 baseline value and the scanning path is unidirectional.
 As a result, the behaviour of the melt pool in these two
 zones is considered as baseline. The melt pool behaviour
 in these zones is labelled as baseline.
- Edge zones: At the edges of the samples, the scanning speed is kept at the baseline value but the laser does a back-and-forth motion to finish a layer and start the next one. Because of this, the deposited heat is locally higher and therefore the thermal condition is different. The melt pool behaviour in these zones is labelled as edge.
- Unlabelled melt pools: Between the three zones defined above, the scanning speed is kept at the baseline value but the melt pool behaviour is assumed to be transient because of the change in the scanning speed. Additionally, the first layers are subjected to the heat sink effect of the thick build plate, which influence the melt pool thermal behaviour. Therefore those melt pools are kept unlabelled to avoid training the model on ambiguous examples.

The three main mechanisms that form defects are (1) keyholes, which come up due to high energy density; (2) gas porosities, which arise from a selective evaporation of an alloy element; and (3) lack of fusion, which are due to a low energy density which prevents the melt pool from reaching the substrate [2]. Hosseini et al. reported that variations of +15% and -15% of energy density around an optimal E_d led

to the apparition of keyholes in the case of the higher energy density and lack of fusion in the case of the lower energy density [40].

The anomaly scanning speeds that were therefore chosen, induce differences in energy densities larger than 15% around the baseline parameters ($E_d=15.69~\mathrm{J/mm^2}$), which insure that they will lead to thermal conditions that are similar to those of defects. The chosen speeds and associated energy densities are listed in table 3. A height difference between the anomaly zone and the baseline zones could be noticed in the 4 samples: the underheat and strong underheat anomaly zones were lower and the overheat and strong overheat zones were higher. This indicates that the local powder efficiency was altered by the speed change and this confirms that the anomaly scanning speed did lead to different thermal conditions.

TABLE 3. Melt pool classes with associated printing parameters and samples.

Melt pool class	v (mm/min)	E_d (J/mm ²)	Scanning path	Sample #
Baseline	900	15.69	Straight	587, 588, 589, 590
Edge	900	15.69	U-turn	587, 588, 589, 590
Underheat	1100	12.83	Straight	587
Strong underheat	1300	10.86	Straight	588
Overheat	700	20.17	Straight	589
Strong overheat	500	28.24	Straight	590

Since the machine position is recorded along with each image, a melt pool class can be linked with each image. Relying on process parameters and the machine position to label the samples instead of material analysis or expert identification, allows to produce a substantial dataset in a limited time and without ex-situ testing costs. This is important to meet the dataset size requirements of DL models and the performance and predictions of DL models can be analysed to iterate on the labelling zones.

C. INFLUENCE OF ENERGY DENSITY ON MICROSTRUCTURE

In order to validate qualitatively the choice of parameters that induce thermal anomalies, micrographs were captured on a selection of samples cut from the printed thin walls described in section II-B. Micrographs allow us to observe the microstructure for the range of energy densities considered for this dataset.

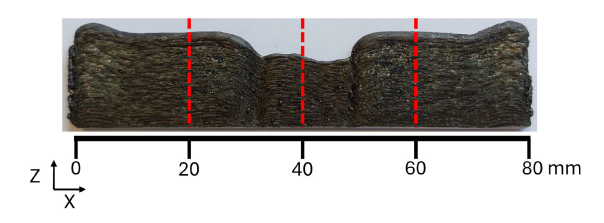
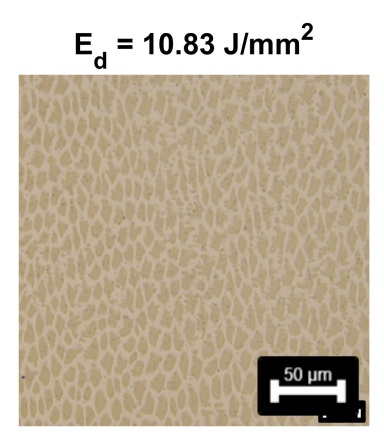
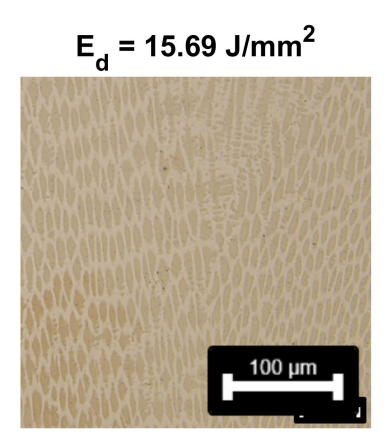


FIGURE 5. Cutting orientation to extract samples from a printed thin wall.







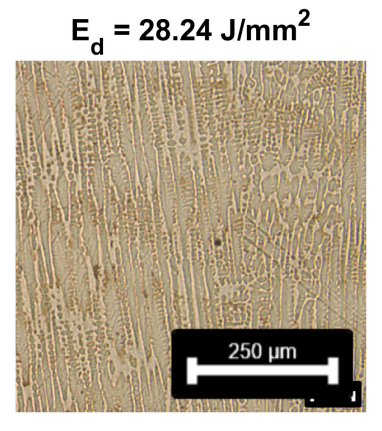


FIGURE 6. Micrographs of thin wall samples for a range of energy densities. The comparison of the micrographs reveal a strong influence link between the local energy density and the shape and orientation of the grains.

Before capturing micrographs, samples were cut from the printed thin walls in the YZ plane at 20, 40 and 60 mm along the length of the thin wall (see fig. 5). Each cut sample was numbered and associated to the local process parameters of the baseline, speed variation or edge zones. The cut samples were then embedded, polished and etched as follows [41]:

- Embedding: The samples were placed in silicon moulds and embedded in a mix of 2/3 Spectrographic black epoxy casting compound and 1/3 hardening agent, following the manufacturer's recommendations. The hardening phase took place in a oven at 50°C for 3 hours.
- 2) **Polishing**: The samples were attached to a circular support frame and placed in a Buehler MOTOPOL 2000 Semiautomatic grinding machine. They were polished in steps of 3 × 3 min periods with increasingly finer grain paper (P180, P320, P600, P1200) and diamond suspension impregnated on a cloth (6 μm, 3 μm and 1 μm). After each 3 min period, the rotational direction of the paper or diamond suspension cloth was reversed with respect to the rotational direction of the samples. After polishing, the samples were cleaned with de-mineralized water.
- 3) **Etching**: The samples were etched for 10 min with Villela reagent (95 ml of ethyl alcohol, 5 ml of hydrochloric acid, and 1 g of picric acid), known to reveal grain boundaries of 316L stainless steel [42]. After etching, the samples were cleaned with de-mineralized water.

Micrographs of the polished samples were captured by Leica DMC2900 USB camera attached to a Leica DMI8-A inverted microscope. Each image was captured in the middle of the sample along the Z axis. The resulting micrographs can be seen in fig. 6, the scale of each image is indicated by a bar in the bottom of each micrograph. Each micrograph reveals the shape and orientation of the grain boundaries associated with the energy density that was used locally.

As can be seen in fig. 6, the lower energy density $E_d = 10.83 \text{ J/mm}^2$ leads to round, small and homogenous grains. On the contrary, the higher energy density E_d 28.24 J/mm² generates bigger, more elongated grains. The intermediate energy density $E_d = 15.69 \text{ J/mm}^2 \text{ produces a}$ median microstructure, bigger and slightly more elongated than the lower energy density. As reported by DebRoy et al., the size and morphology of the DED microstructure is determined by the combined effects of the temperature gradient and the solidification rate during the successive layers [5]. In our case, the micrographs demonstrate that the chosen range of energy densities has a large effect on the microstructure. The observed microstructures of $E_d = 10.83$ J/mm^2 and $E_d = 28.24 J/mm^2$ are typical of conditions where lack-of-fusion and keyhole defects are respectively likely, as reported by literature [33], [43]. This observation does not guarantee the presence of defects but it indicates that the melt pool signatures for those parameters are typical of undesirable thermal conditions.

D. DATASET AND PRE-PROCESSING

The raw dataset consists of 561 861 hyperspectral images coming from four thin wall samples and distributed among 6 classes [36]. Each image is associated with the position of the machine when the image was recorded and therefore with a melt pool class depending on the local printing parameters and thermal conditions, as explained in the last section. The distribution of images among the classes can be seen in fig. 7. The dataset is clearly unbalanced. All four samples contain baseline and edge zones and therefore there are more images belonging to those classes than the anomaly classes. This dataset must undergo three separate steps before it can be used by DL models: a step that separates training and validation data, a step that balance classes and a step that pre-processes images.

First, to avoid the risk of over-fitting a model to the particular set of available data, the dataset is randomly split in two parts: one part for the training set (70%, 393 303 images)

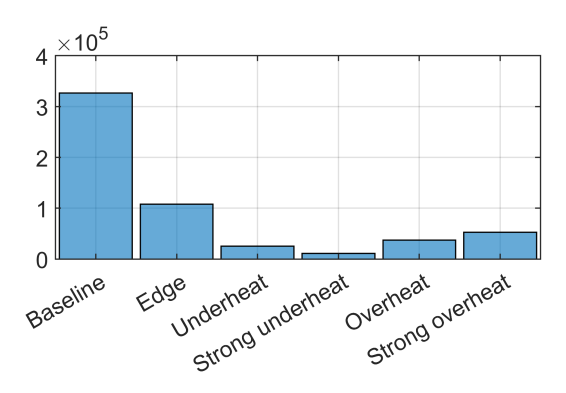


FIGURE 7. Histogram of the raw dataset showing a clear class imbalance. The minority classes are oversampled before the data is fed to DL models to counteract the imbalance.

and one part for the validation set (30%, 168 558 images). The images are randomly selected across the four samples and the 6 classes during this step. At this stage, the two parts are still unbalanced.

Then, to avoid a bias towards the majority class of this unbalanced dataset (in this case predicting a baseline melt pool too often), weighted sampling is used to produce balanced training and validation sets. This method consists in assigning a probability weight to each image and then images are randomly drawn from each set depending on their weights. Typically, images from minority classes are given higher weights, meaning they are more likely to be selected during the sampling process. As a result, even though the initial dataset is unbalanced, weighted sampling compensates by selecting samples from minority classes more frequently and samples from the majority class less frequently, thus creating balanced training and validation sets to use to train the DL model. This technique is applied separately to the training and validation set to keep the training and validation data separated. In order to keep training times reasonable under the computational constraints that were faced, 100 000 images were drawn for the balanced training set and 10 000 images for the balanced validation set.

Finally, the hyperspectral images are preprocessed to promote optimal learning by the DL models. The image pre-processing operations are illustrated in fig. 8. First, raw hyperspectral images are debayered, as described in section II-A. Practically, each 250×250 raw hyperspectral image is reshaped into a 25 \times 49 \times 49 cubic structure. The pixel values in themselves are not modified, only the data structure is changed. For illustration purposes, a single 49×49 slice is shown in fig. 8, but the entire cubic structure is used as input for the DL model. A misalignment exists between the macropixels at the edge of the raw image and the borders of the raw image, incomplete macropixels are therefore discarded during the debayering operation. This is the reason why there are a few less pixels in the debayered cubic structure than in the raw hyperspectral image. After the debayering operation, the images are randomly rotated. The angle of rotation of the image is chosen at random

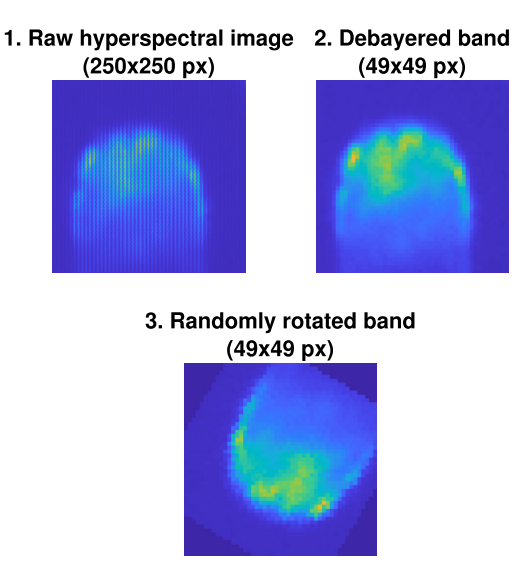


FIGURE 8. Pre-processing operations applied to hyperspectral images before feeding them to DL models. The debayered band used for this figure is centred at the peak wavelength $\lambda = 784 \, nm$.

between -180 and 180 degrees at the code execution. The objective of this second operation is to avoid a bias towards the orientation of the melt pool images in the thin wall samples (unidirectional). It is a standard practice in DL.

E. STRUCTURE OF THE CLASSIFICATION MODEL

In this section, the structure of the classification model is described and the training parameters are detailed.

To build a model of the relationship between the melt pool NIR signature (hyperspectral image) and the categorical melt pool class, a Supervised Learning classification algorithm is used. As explained in the introduction, Convolutional Neural Networks (CNN) are well adapted to image classification tasks thanks to their translation invariance through weight sharing of the convolutional filters and local connectivity that takes the spatial structure of images into account [29]. In addition, CNN are able to accommodate and make efficient use of the large number of input channels (camera wavelength bands) of debayered hyperspectral images [35].

Three different CNN structures are considered: a baseline CNN architecture and two ResNet architectures, ResNet-18 and ResNet-50 [30]. The convolutional operation used in this work is the well-known 2D spatial convolution [29], [30]. For all 3 architectures, the first convolutional layer takes the 25 wavelength bands of the hyperspectral image as input into 25 channels and the last fully connected layer outputs logits for 6 classes. The baseline architecture is only made of convolutional, pooling, activation and fully connected layers (see table 4). The ResNet architecture uses batch normalization and residual layers in addition to avoid vanishing gradients and to allow the convergence of a deeper network. This architecture is well regarded and has been used in many recent metal AM applications [44], [45], even though more modern evolutions such as Inception-ResNet have been



reported [46]. The ResNet-18 and ResNet-50 architectures respectively make use of 18 and 50 convolutional and fully connected layers in total. The depth and number of parameters of the three architectures are compared in table 6. The main differences between the ResNets and the baseline CNN are the absence of residual layers and a lower capacity for the baseline CNN.

TABLE 4. Baseline CNN architecture showing the depth and width of the feature extraction and classification layers.

Layer	Sublayers	Output size
Conv1	Conv2D: kernel=5x5, stride=1 ReLU MaxPool2D: kernel=2x2, stride=2	[64,45,45] [64,45,45] [64,22,22]
Conv2	Conv2D: kernel=5x5, stride=1 ReLU MaxPool2D: kernel=2x2, stride=2	[128,18,18] [128,18,18] [128,9,9]
Flatten		[10368]
FC1	Linear: output=6	[6]

TABLE 5. Hyperparameters used to train the CNN models.

Cost function	Cross-entropy
Optimizer	Adam
Learning rate	5×10^{-5}
Batch size	256
Max. number of epochs	300
Early stopping patience	10 epochs

The three architectures are implemented with PyTorch 2.0.1 and are trained on the described dataset with the hyperparameters listed in table 5. Weight initialization is random. Early stopping was implemented to avoid training the model for more epochs than necessary: if the loss does not decrease for more than an amount of epochs, the training is stopped. The criterium for the number of epochs without loss improvement is called patience.

III. RESULTS AND DISCUSSION

A. MODEL CAPACITY AND PERFORMANCE METRICS

In this section, the performance of the various structures described in section II-E is discussed.

The training curves can be seen in fig. 9. In this plot, the training accuracy and loss are plotted with solid lines and validation accuracy and loss are plotted with lines with periodic triangular markers (△). At the plot scale, the training and validation curves are overlapping, which indicates that the training process is successfully progressing towards generalization. Table 6 shows the accuracies on the test set obtained after training each architecture. The ResNet-18 and ResNet-50 have similar accuracy above 94%, clearly outperforming the CNN baseline which is at 81%. The higher capacity of the ResNet architecture led to a lower bias without overfitting. The ResNet-18 and ResNet-50 have a nearly identical performance, despite the ResNet-50 architecture

having many more trainable parameters. This is probably due to the inherent learning task contained in the data and not due to a capacity limitation. Compared to the state-of-the-art defect classification models using monochrome images in DED and LPBF (see table 1), the multiclass classification architectures proposed in this work achieve a similar accuracy to binary models and a higher accuracy than other multiclass models. It should be noted that learning tasks involving hyperspectral data with a larger number of bands required a more modern architecture such as Inception-ResNet [47], [48]. While the ResNet architecture is sufficient for the learning task presented in this work, the Inception-ResNet architecture might be of interest for future, more complex learning tasks in DED.

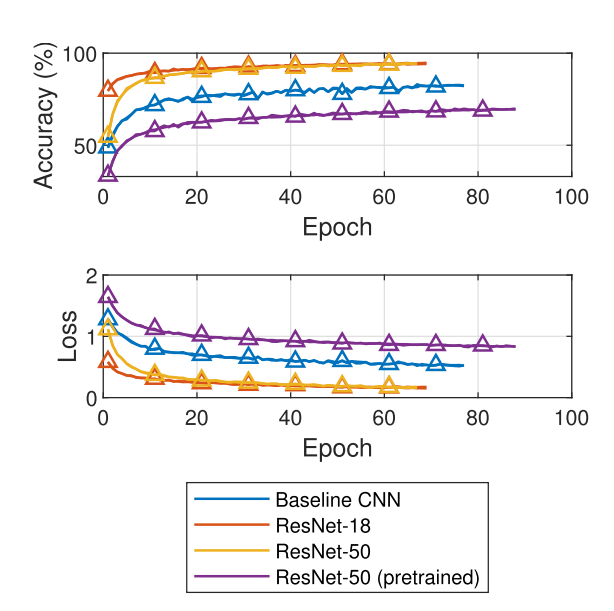


FIGURE 9. Training curves: training accuracy and loss are plotted with solid lines and validation accuracy and loss are plotted with lines with periodic markers. At the plot scale, the training and validation curves are overlapping, which indicates that the training process is successfully progressing towards generalization. The ResNet-18 and ResNet-50 obtain the best performance over the validation set.

TABLE 6. Performance metrics and characteristics of the three CNN architectures. The ResNet-18 architecture shows the best balance between accuracy and inference time.

Model	Baseline CNN	ResNet-18	ResNet-50
# conv. and f.c. layers	3	18	50
Trainable parameters	307 206	11 248 069	23 587 269
Accuracy on test set (%)	81.0	94.1	94.2
Inference time (ms)	0.74	4.51	7.57

Additionally, the inference time (time to make a prediction on a hyperspectral image) is proportional to the number of parameters of the CNN models (table 6), as expected. The ResNet-18 architecture is able to achieve almost the same accuracy as the ResNet-50 while taking only 5ms to make a prediction. All inference times were computed on a Intel Core i7-9850H and a NVIDIA Quadro RTX 3000. For comparison,



Snyers et al. reported a computational time of $32 \, \mathrm{s}$ to estimate the temperature distribution of a 300×300 hyperspectral image using the multicolor pyrometry method on a modern 6-core CPU [27]. This highlights the efficiency and potential of the proposed model in handling complex and large-scale hyperspectral data in real-time.

The dynamic model of the DED melt pool width may be approximated by a first-order transfer function G(s) with a time constant τ [49]:

$$G(s) = \frac{K}{1 + \tau s} \tag{2}$$

Akbari et al. estimated the time constant of this dynamic model between 100 and 250 ms for a range of process conditions [49]. Controlling the DED process would require a sampling time an order of magnitude lower than the process time constant, which corresponds to an sampling time of 10ms in the worst case. The inference time of the anomaly classification model proposed in this work is compatible with such a constraint and should allow its integration in a closed loop control framework with reasonable hardware requirements.

In addition to the three architectures with randomly initialized weights, a second ResNet-50 CNN is considered with pre-trained IMAGENET1K-V1 weights for all inner layers. The goal of using pretrained weights is to re-use knowledge learned from a task to boost performance on a related task. In this case, the pretrained weights result from training a ResNet-50 CNN on the ImageNet 2012 dataset [30]. This dataset contains 1.28 million images distributed in 1000 classes.

The inner layers use pre-trained and frozen weights and the first and last layers are modified as described in section II-E. As a result, training the CNN only has an effect on the first and last layers. The learning rate is reduced to 1×10^{-5} to avoid oscillations in training. As can be seen in fig. 9, the accuracy of the pre-trained network tops at 69% and after 88 epochs the training stopped because the early stopping criterium is reached. The lack of improvement over random initialization could indicate that the domain gap between the original dataset (ImageNet) and the melt pool hyperspectral signatures is too big. Knaak et al. made the same observation when trying to re-train a ResNet-50 model with LPBF powder bed images [50].

To conclude, the ResNet-18 architecture with randomly initialized weights reaches an accuracy of over 94%, which is equivalent to the ResNet-50 accuracy while having a lower inference time. This accuracy exceeds the performance of other multiclass anomaly detection models applied to DED or LPBF data. The ResNet-18 architecture is therefore chosen as the proposed model for the rest of this work.

B. CONFUSION MATRIX

In this section, the performance of the proposed classification model is evaluated and analysed per-class on the validation subset of the described dataset.

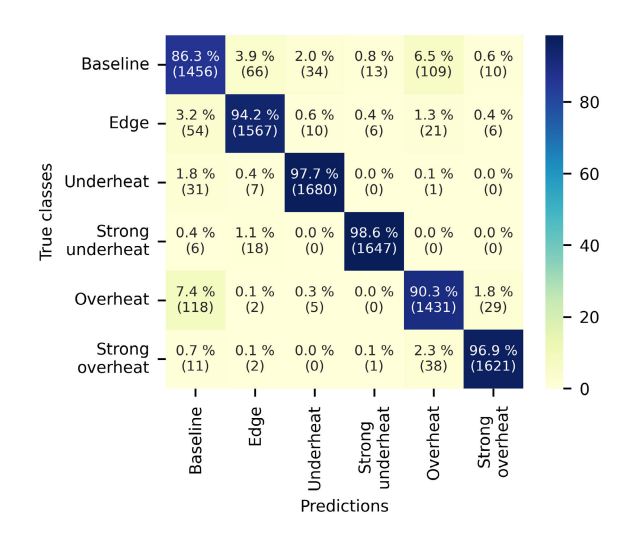


FIGURE 10. Normalized and cumulative confusion matrix for the proposed model applied on a 10 000 samples subset of the validation set. The matrix is normalized per row (dividing by the number of true instances per class). This figure helps localize the classes that cause the most misclassifications.

The normalized and cumulative confusion matrix is depicted in fig. 10 and shows the correct and incorrect classifications per class for the validation set. The numbers between brackets are the absolute numbers of instances and the normalized values are obtained by dividing the number of instances in each square by the number of true instances per class. The rates on the matrix main diagonal are the class recall rates since the matrix is normalized per row. The recall rate for the baseline class is 86.3% and above 90% for the other classes. The main source of error comes from overheat-baseline misclassification which impacts the baseline recall rate and which will be investigated in the sample 589 prediction plot in section III-C. The overall accuracy of the classification model reaches a satisfactory performance and confirms that the anomaly dataset labelled with process anomalies contain differentiable melt pool signatures.

C. 2D PREDICTION PLOTS

Beyond the accuracy of a single image classification, the model predictions should be viewed in the physical context of the thin wall sample and compared to the ground truth.

Fig. 11 shows the ground truth and model predictions of sample 590, which was printed with a strong overheat anomaly. The upper plot depicts the location of the labelled and unlabelled zones as described in section II-B. As explained previously, scanning speed changes happen at two precise locations along the X axis, but melt pool close to the change of speed are kept unlabelled because they are suspected to be in a transient state. The lower plot depicts the model predictions, which are plotted with their respective machine positions in the XZ plane. Such plots allow to analyse the distribution of correct and wrong



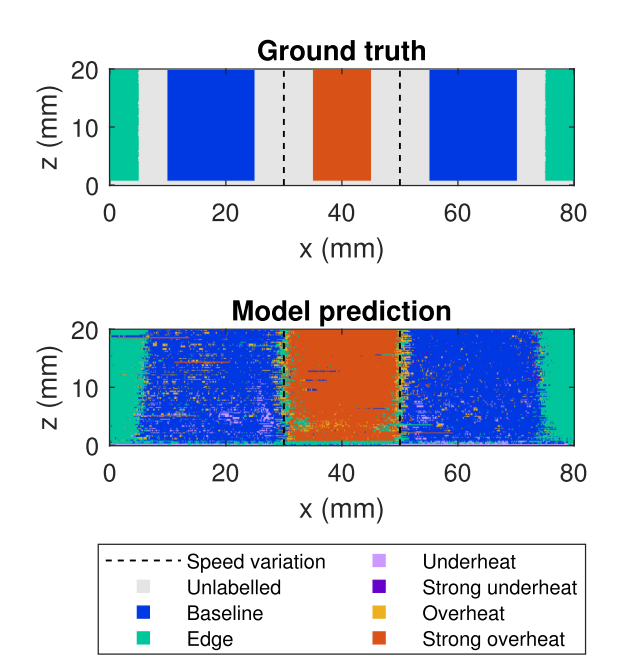
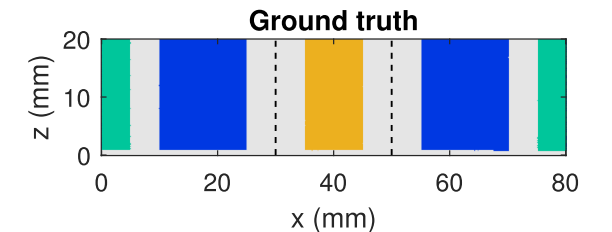


FIGURE 11. Sample 590 ground truth and prediction plot. The predictions are plotted with their respective machine positions in the XZ plane. This figure shows clustered predictions that are in good agreement with the ground truth.

predictions in the zones with labelled data and compare the model predictions for the unlabelled sample areas with our expectations from a physical point of view.

We can see in the lower plot of fig. 11 that the classification model correctly identifies the edge, baseline and strong overheat regions. This shows practically that the proposed model behaves as expected. The classifications errors are mainly located in the baseline zones and are small clusters of overheat or underheat melt pools. They are composed of only a few images. The time constant of the melt pool under similar process parameters is approximately 200 ms [49] and indicates if there was a change of melt pool behaviour, the camera functioning at 500 Hz would record the transition in approximately 100 images. Therefore, error clusters of a couple of images in fig. 11 are probably coming from the classification model and not a physical change in melt pool behaviour. Such small error clusters could be removed by using a moving average over the class predictions. Additionally, it should be noted that the model classifies the full first layer as "underheat". This makes sense physically because at the first layer the laser shines a stainless steel build plate of several centimetres. This big object comparatively to the thin wall acts as a heat sink and reduces the size of the melt pool. In the unlabelled regions between edge and baseline and between baseline and the speed anomaly zone, we can see a rather smooth transition from one class prediction to the other, which confirms the transient assumption made in section II-B.

Fig. 12 shows the prediction plot of sample 589, which was printed with a overheat anomaly. We can see similar small error clusters as in fig. 11, but also longer lines of



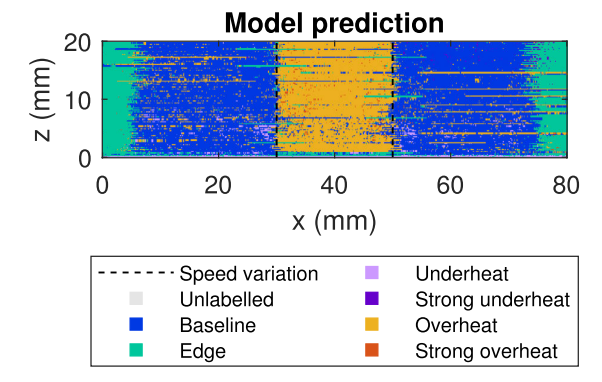


FIGURE 12. Sample 589 ground truth and prediction plot. The predictions are plotted with their respective machine positions in the XZ plane. The figure shows localized errors, mainly in the overheat and baseline regions.

overheat melt pool in the baseline zones. The length of those overheat classifications is sufficient to indicate a physical change in the melt pool behaviour. Those misclassifications with respect to the ground truth explain the high error rate in the overheat-baseline case of the confusion matrix, as noted in section III-B. This high error rate combined with the long "line" clusters could indicate that this anomaly actually occurs spontaneously in the sample and might be triggered by either the edge or the speed anomaly transients.

The high accuracy of the model described in section III-B, coupled with its successful identification of anomaly zones as demonstrated in fig. 11 and fig. 12, underscores the effectiveness of the CNN-based approach in detecting and classifying DED anomalies using high-dimensional hyperspectral data. In contrast to existing data-driven DED anomaly classification models discussed in section I (see table 1), which are limited to binary classification, the model presented in this work represents a significant advancement. It not only differentiates among multiple DED anomaly classes but also establishes a direct link between hyperspectral data and these classes. Concretely, this means that such a model is able to detect a specific kind of defect during printing by measuring the IR signature of the melt pool independently from the printed shape. Appropriate action could be taken to correct the defect as it is detected, depending on the type of defect.

To summarize, the proposed model is able to detect overall ground truth regions accurately and the predictions in the unlabelled zones are linked to physical phenomena. This model exceeds the capabilities of state-of-the-art models identified in section I.



D. PRELIMINARY INSPECTION WITH SALIENCY MAPS

1) CLASS ACTIVATION MAPS

In this section, the model classification mechanism is investigated with the help of visualization methods.

Although a Deep Learning model is usually considered as a black box, there has been significant effort in the field of Explainable AI to understand how CNN reach their predictions. Gradient-weighted Class Activation Mapping (GradCAM) and guided backpropagation are two visualization methods that produce a heat-map that shows which part of an image is used by a network to make a prediction [51], [52]. Guided backpropagation is able to highlight individual pixels based on their contribution to the output through the network, but is not class discriminative. In contrast, GradCAM is class discriminative but produces a coarser localization map by only highlighting convolutional feature maps (7×7) for the last layer of a ResNet-50 CNN [30]) and not single pixels. To obtain a localization map that is both fine-grained and class discriminative, Selvaraju et al. proposed to combine the two methods into the Guided GradCAM method [51]. This is the method used in this work.

Fig. 13 shows 6 melt pool images (only a single band is shown per melt pool hyperspectral image for clarity, i.e. one slice from the 3D structure presented in fig. 1), each belonging to a different class, and their associated Guided GradCAM localization maps. The laser is moving in the same direction (upwards on the plot) in all melt pool images to facilitate the analysis and the proposed model correctly predicts each of the classes for those 6 images. All melt pool images and localization maps are normalized to [0,1] for better readability. The localization maps show which pixels in the original image make the most contribution for the model to make its (correct) prediction. GradCAM-based maps are known to often be noisy and visually-sharp. Smilkov et al. identified noise in GradCAM maps as meaningless, noisy variations in gradients [53]. Based on this, the localization maps presented in this work have been post-treated with a simple 2D Gaussian filter ($\sigma = 3$) to improve readability and interpretability. The standard deviation (or width) of the filter was used as a tuning parameter and was optimized visually.

We can see in fig. 13 that each class has a different fingerprint in its localization map. The 6 classes can be divided in three groups based on their localization map and their energy input. A potential link between the fingerprints and the physical temperature distribution in the melt pool can be proposed:

- For the baseline and edges classes, the model focuses on the melt pool front edge, where the pixel values are higher because of the higher temperature than in the tail. A broad leading edge could be a specific characteristic of those two classes. The model additionally looks at the unstable features happening in the edge image, caused by the change of direction.
- For the underheat and strong underheat classes, the model looks at the centre of the melt pool. The melt pool

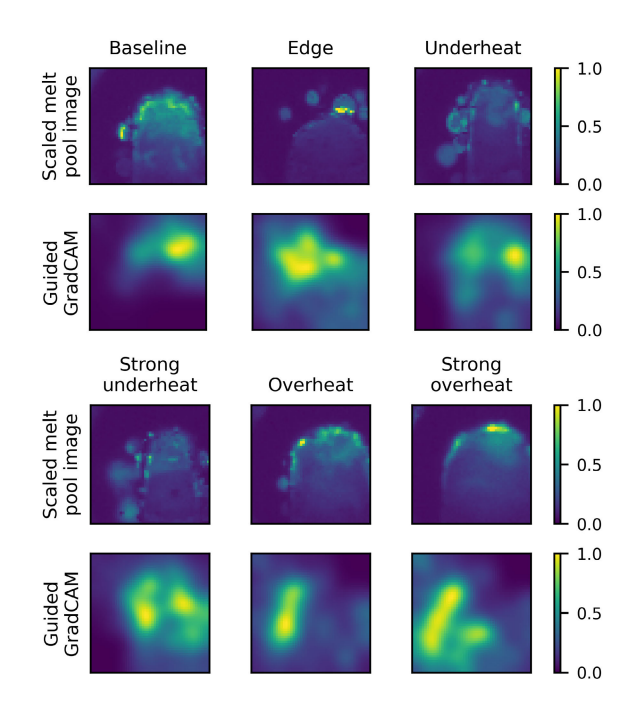


FIGURE 13. Melt pool NIR signature (794 nm band) and associated CAM for each class of the classification model. Each class shows a specific signature on its CAM.

visible left side is thinner for those classes because of the lower energy input and this could be a discriminative factor for the model. We can also see that the model looks outside of the melt pool area to the left. The model could probably be looking for bright spots caused by spatter or powder particles, which are visible on the strong underheat image for example.

• For the overheat and strong overheat, the model looks very specifically at the left-side edge of the melt pool. The pixel values are more likely to be high over those 2 locations for those classes because of the higher energy input. A well-defined and wide left-side edge could therefore be a discriminative factor for higher energy inputs. Additionally, the model looks at the melt pool centre only for the strong overheat class. In addition to the first criterion, higher values in the centre could be the discriminative factor between overheat and strong overheat.

It should be noted that the GradCAM maps are only valid for the 6 images shown and that the link between the discriminative regions and the temperature distributions has not been validated. Future work should be conducted to validate the link between physical features and black-box model predictions.

To summarize, the Guided GradCAM method showed different discriminative regions for each of the melt pool classes, equivalent to a different signature for each class. Melt pools that are thermally close have a similar signature



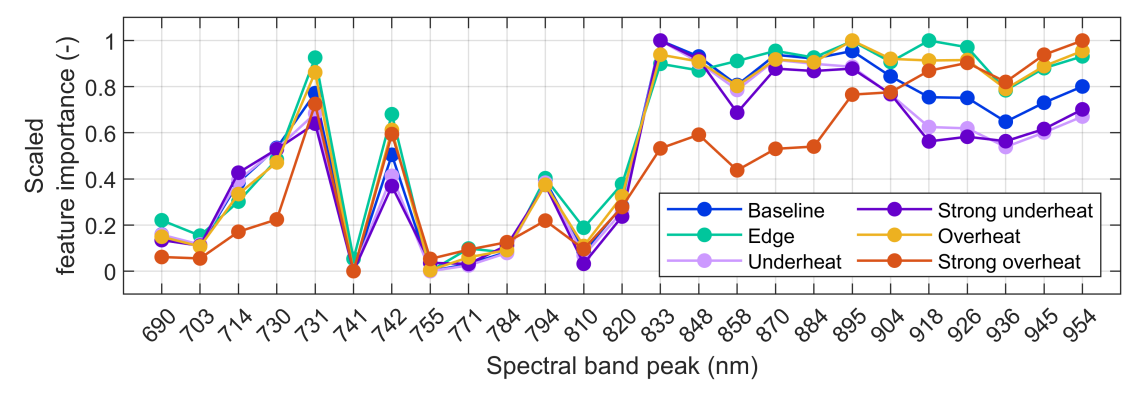


FIGURE 14. Feature importance per spectral band and per class of the test set melt pool images. This plot shows that many bands are significant for the classification model regardless of the class, demonstrating the interest of hyperspectral data.

and a potential link between melt pool signatures and the temperature distributions is proposed.

2) SPECTRAL BAND ANALYSIS

In addition to the analysis of the significance of spatial regions with Class Activation Maps, it is of interest to study the importance of the spectral bands to the classification model given the necessary overhead to process them. A spectral feature importance metric $FI(\lambda, c)$ is computed for each spectral band λ and class c. It was obtained by generating GradCAM maps $L_{GradCAM}^c$ for all test set images, averaging each map over the spatial pixels (i, j) and sum the averages for all images n_c belonging to the same class c:

$$FI(\lambda, c) = \sum_{n_c} \left(\frac{\sum_i \sum_j L_{GradCAM}^c(i, j, \lambda)}{N} \right)$$
 (3)

with $L^c_{GradCAM}(i, j, \lambda)$ the GradCAM value at pixel (i, j) and spectral band λ for class c and N the number of pixels per spectral band.

The spectral feature importance vector is then rescaled to the [0, 1] interval to easily compare the relative importance of each spectral band from one class to another. The resulting metric is shown in fig. 14. The plot shows clearly that many bands are significant for the classification model regardless of the class, demonstrating the interest of hyperspectral data for the anomaly classification task presented in this work. Additionally, it can be seen that the bands centered around wavelengths over 820 nm have a higher feature importance than the bands centerend around wavelengths under this length. Retrain a smaller network with only spectral bands above 820 nm could lead to a similar performance to the model presented in section III-A with a faster inference speed. Finally, we can observe that, while the significant spectral bands are mostly the same for each class, the relative value of each band varies per class, leading to a different spectral fingerprint for each class.

To summarize, the spectral metric proposed in this section shows that several bands appear to be meaningful to the classification model, which proves the benefit of

hyperspectral IR data for this application. In future work, a smaller model which only takes the most significant spectral bands as input, could be trained and compared to the model proposed in this work.

IV. CONCLUSION

The main contributions of this work are:

- Dataset and labelling method: An experimental anomaly dataset of over 500 000 hyperspectral melt pool NIR signatures and a labelling method relying on process parameters were presented. A qualitative analysis of the microstructure was performed over the range of considered energy densities, indicating that the chosen parameters result in typical undesirable thermal conditions. The main advantage of the proposed labelling method is meeting the data requirements of DL methods without costly material analysis or expert identification on every sample.
- Anomaly classification model: A classification model using hyperspectral data and a CNN architecture is proposed. It was able to reach an accuracy of over 94% on the validation set, an improvement over state-of-theart models. The error rate of the model was analysed per class and potential paths for improvements were identified.
- Real-Time application feasibility: The inference speed of the model was measured under 5 ms, making it suitable for real-time applications. This performance significantly outperforms conventional multicolor pyrometry in computational efficiency.
- Preliminary inspection with Guided GradCAM:
 The Guided GradCAM method was used to visualize relevant regions in melt pool images, revealing that the model considers different regions for each class. Additionally, an spectral feature importance metric was computed by averaging GradCAM maps over the spatial dimensions. This metric demonstrated the benefit of hyperspectral data for melt pool anomaly classification.

For future work, more complex anomaly samples should be printed to assess further the performance of the model



and anomaly classification should be integrated in a real-time closed loop framework to apply a corrective action to the detected process anomalies. Additionally, the link between temperature distribution and the melt pool discriminative regions for classification should be investigated to better explain how the model classify melt pools. A smaller model which only takes the most significant spectral bands as input, could be trained and compared to the model proposed in this work.

DATA AVAILABILITY STATEMENT

The data that support the findings of this study are openly available on Zenodo at https://doi.org/10.5281/zenodo. 10409569.

REFERENCES

- C. Snyers, J. Ertveldt, J. Sanchez-Medina, Z. Jardon, and J. Helsen, "Prediction of build geometry for DED using supervised learning methods on simulated process monitoring data," *J. Laser Appl.*, vol. 33, no. 4, Nov. 2021, Art. no. 042052.
- [2] D. Svetlizky, M. Das, B. Zheng, A. L. Vyatskikh, S. Bose, A. Bandyopadhyay, J. M. Schoenung, E. J. Lavernia, and N. Eliaz, "Directed energy deposition (DED) additive manufacturing: Physical characteristics, defects, challenges and applications," *Mater. Today*, vol. 49, pp. 271–295, Oct. 2021.
- [3] P. R. Gradl, "Principles of directed energy deposition for aerospace applications," in *Drive AM Industry Connect Meeting*. AL, USA: NASA, Marshall Space Flight Center Redstone Arsenal, Jan. 2021.
- [4] E. Toyserkani, A. Khajepour, and S. Corbin, *Laser Cladding*. Boca Raton, FL, USA: CRC Press, 2005.
- [5] T. DebRoy, H. L. Wei, J. S. Zuback, T. Mukherjee, J. W. Elmer, J. O. Milewski, A. M. Beese, A. Wilson-Heid, A. De, and W. Zhang, "Additive manufacturing of metallic components—Process, structure and properties," *Prog. Mater. Sci.*, vol. 92, pp. 112–224, Mar. 2018.
- [6] F. Marin, A. F. de Souza, A. Mikowski, L. H. G. Fontanella, P. Soares, and L. N. L. de Lacalle, "Energy density effect on the interface zone in parts manufactured by laser powder bed fusion on machined bases," *Int. J. Precis. Eng. Manuf.-Green Technol.*, vol. 10, no. 4, pp. 905–923, Jul. 2023.
- [7] H. L. Wei, T. Mukherjee, W. Zhang, J. S. Zuback, G. L. Knapp, A. De, and T. DebRoy, "Mechanistic models for additive manufacturing of metallic components," *Prog. Mater. Sci.*, vol. 116, Feb. 2021, Art. no. 100703.
- [8] W. Yan, S. Lin, O. L. Kafka, Y. Lian, C. Yu, Z. Liu, J. Yan, S. Wolff, H. Wu, E. Ndip-Agbor, M. Mozaffar, K. Ehmann, J. Cao, G. J. Wagner, and W. K. Liu, "Data-driven multi-scale multi-physics models to derive process-structure-property relationships for additive manufacturing," *Comput. Mech.*, vol. 61, no. 5, pp. 521–541, May 2018.
- [9] W. Devesse, D. De Baere, and P. Guillaume, "High resolution temperature measurement of liquid stainless steel using hyperspectral imaging," *Sensors*, vol. 17, no. 1, p. 91, Jan. 2017.
- [10] M. Lison, W. Devesse, D. de Baere, M. Hinderdael, and P. Guillaume, "Hyperspectral and thermal temperature estimation during laser cladding," J. Laser Appl., vol. 31, no. 2, May 2019, Art. no. 022313.
- [11] S. J. Altenburg, A. Straße, A. Gumenyuk, and C. Maierhofer, "Insitu monitoring of a laser metal deposition (LMD) process: Comparison of MWIR, SWIR and high-speed NIR thermography," *Quant. Infr. Thermography J.*, vol. 19, no. 2, pp. 97–114, Mar. 2022.
- [12] W. Devesse, D. De Baere, M. Hinderdael, and P. Guillaume, "Model-based temperature feedback control of laser cladding using high-resolution hyperspectral imaging," *IEEE/ASME Trans. Mechatronics*, vol. 22, no. 6, pp. 2714–2722, Dec. 2017.
- [13] J. Ertveldt, J. Sanchez-Medina, Z. Jardon, M. Hinderdael, and P. Guillaume, "Experimental identification of process dynamics for real-time control of directed energy deposition," *Proc. CIRP*, vol. 111, pp. 321–325, Jan. 2022.
- [14] J. Sanchez-Medina, D. De Baere, C. Snyers, Z. Jardon, M. Hinderdael, J. Ertveldt, and P. Guillaume, "Comparison and analysis of hyperspectral temperature data in directed energy deposition," *J. Laser Appl.*, vol. 35, no. 4, Oct. 2023, Art. no. 042037.

- [15] S. K. Everton, M. Hirsch, P. Stravroulakis, R. K. Leach, and A. T. Clare, "Review of in-situ process monitoring and in-situ metrology for metal additive manufacturing," *Mater. Des.*, vol. 95, pp. 431–445, Apr. 2016.
- [16] G. Tapia and A. Elwany, "A review on process monitoring and control in metal-based additive manufacturing," *J. Manuf. Sci. Eng.*, vol. 136, no. 6, Oct. 2014, Art. no. 060801.
- [17] Z. Y. Chua, I. H. Ahn, and S. K. Moon, "Process monitoring and inspection systems in metal additive manufacturing: Status and applications," *Int. J. Precis. Eng. Manuf.-Green Technol.*, vol. 4, no. 2, pp. 235–245, Apr. 2017.
- [18] M. Khanzadeh, S. Chowdhury, M. A. Tschopp, H. R. Doude, M. Marufuzzaman, and L. Bian, "In-situ monitoring of melt pool images for porosity prediction in directed energy deposition processes," *IISE Trans.*, vol. 51, no. 5, pp. 437–455, May 2019.
- [19] B. Zhang, S. Liu, and Y. C. Shin, "In-process monitoring of porosity during laser additive manufacturing process," *Additive Manuf.*, vol. 28, pp. 497–505, Aug. 2019.
- [20] Q. Tian, S. Guo, E. Melder, L. Bian, and W. Guo, "Deep learning-based data fusion method for in situ porosity detection in laser-based additive manufacturing," *J. Manuf. Sci. Eng.*, vol. 143, no. 4, Dec. 2020, Art. no. 041011.
- [21] B. Abranovic, S. Sarkar, E. Chang-Davidson, and J. Beuth, "Melt pool level flaw detection in laser hot wire directed energy deposition using a convolutional long short-term memory autoencoder," *Additive Manuf.*, vol. 79, Oct. 2023, Art. no. 103843.
- [22] X. Li, S. Siahpour, J. Lee, Y. Wang, and J. Shi, "Deep learning-based intelligent process monitoring of directed energy deposition in additive manufacturing with thermal images," *Proc. Manuf.*, vol. 48, pp. 643–649, Jan. 2020.
- [23] S. Oster, P. P. Breese, A. Ulbricht, G. Mohr, and S. J. Altenburg, "A deep learning framework for defect prediction based on thermographic in-situ monitoring in laser powder bed fusion," *J. Intell. Manuf.*, vol. 35, no. 4, pp. 1687–1706, May 2023.
- [24] L. Scime and J. Beuth, "Using machine learning to identify in-situ melt pool signatures indicative of flaw formation in a laser powder bed fusion additive manufacturing process," *Additive Manuf.*, vol. 25, pp. 151–165, Jan. 2019.
- [25] C. Knaak, J. von Eßen, M. Kröger, F. Schulze, P. Abels, and A. Gillner, "A spatio-temporal ensemble deep learning architecture for real-time defect detection during laser welding on low power embedded computing boards," *Sensors*, vol. 21, no. 12, p. 4205, Jun. 2021.
- [26] W. Cai, P. Jiang, L. Shu, S. Geng, and Q. Zhou, "Real-time identification of molten pool and keyhole using a deep learning-based semantic segmentation approach in penetration status monitoring," *J. Manuf. Processes*, vol. 76, pp. 695–707, Apr. 2022.
- [27] C. Snyers, J. Ertveldt, J. Sanchez-Medina, Z. Jardon, and J. Helsen, "Prediction of melt pool temperature for directed energy deposition using supervised learning methods on optical measurement data," in *Progress* in Additive Manufacturing 2021. West Conshohocken, PA, USA: ASTM International, 2022, pp. 59–73.
- [28] I. Goodfellow, Y. Bengio, and A. Courville, *Deep Learning*. Cambridge, MA, USA: MIT Press, 2016.
- [29] A. Krizhevsky, I. Sutskever, and G. E. Hinton, "ImageNet classification with deep convolutional neural networks," *Commun. ACM*, vol. 60, no. 6, pp. 84–90, May 2017.
- [30] K. He, X. Zhang, S. Ren, and J. Sun, "Deep residual learning for image recognition," in *Proc. IEEE Conf. Comput. Vis. Pattern Recognit. (CVPR)*, Jun. 2016, pp. 770–778.
- [31] Y. Zhang, J. Y. H. Fuh, D. Ye, and G. S. Hong, "In-situ monitoring of laser-based PBF via off-axis vision and image processing approaches," *Additive Manuf.*, vol. 25, pp. 263–274, Jan. 2019.
- [32] N. Gerdes, C. Hoff, J. Hermsdorf, S. Kaierle, and L. Overmeyer, "Hyperspectral imaging for prediction of surface roughness in laser powder bed fusion," *Int. J. Adv. Manuf. Technol.*, vol. 115, no. 4, pp. 1249–1258, Jun. 2021.
- [33] A. Saboori, A. Aversa, G. Marchese, S. Biamino, M. Lombardi, and P. Fino, "Microstructure and mechanical properties of AISI 316L produced by directed energy deposition-based additive manufacturing: A review," Appl. Sci., vol. 10, no. 9, p. 3310, May 2020.
- [34] A. Aversa, G. Marchese, and E. Bassini, "Directed energy deposition of AISI 316L stainless steel powder: Effect of process parameters," *Metals*, vol. 11, no. 6, p. 932, Jun. 2021.



- [35] C. Snyers. (Sep. 2023). Deep Learning Anomaly Detection in Directed Energy Deposition Using Hyperspectral in-Situ Monitoring Data. [Online]. Available: https://researchportal.vub.be/en/activities/deep-learning-anomaly-detection-in-directed-energy-deposition-usi
- [36] C. Snyers, J. Ertveldt, and J. Helsen, "Dataset of hyperspectral melt pool signatures and thermal anomalies in DED of 316L steel," Vrije Universiteit Brussel, Brussels, Belgium, Tech. Rep., 2023, doi: 10.5281/zenodo.10409569.
- [37] J. Ertveldt, P. Guillaume, and J. Helsen, "MiCLAD as a platform for realtime monitoring and machine learning in laser metal deposition," *Proc. CIRP*, vol. 94, pp. 456–461, Jan. 2020.
- [38] M. Planck, Vorlesungen Über Die Theorie Der Wärmestrahlung. Leipzig, Germany: J. A. Barth, 1913.
- [39] W. Devesse, "Development and validation of innovative modeling, monitoring and control strategies for 3D metal printing," Ph.D. thesis, Dept. Mech. Eng., Vrije Universiteit Brussel, Brussels, Belgium, Feb. 2017.
- [40] S. Hosseini, A. Shmatok, B. Prorok, and E. Mirkoohi, "Criticality of volumetric defect structure on fatigue properties of stainless steel 316L fabricated by laser powder direct energy deposition," *J. Manuf. Processes*, vol. 127, pp. 259–273, Oct. 2024.
- [41] Z. Jardon, "Numerical and experimental study of a crack localisation system embedded in 3D printed smart metallic components," Ph.D. thesis, Dept. Mech. Eng., VUBPRESS, Brussel, Belgium, 2022.
- [42] G. F. Vander Voort, G. M. Lucas, and E. P. Manilova, "Metallography and microstructures of stainless steels and maraging steels," in *Metallography* and *Microstructures*, G. F. Vander Voort, Ed., West Conshohocken, PA, USA: ASM International, 2004, pp. 670–700.
- [43] B. Zheng, J. C. Haley, N. Yang, J. Yee, K. W. Terrassa, Y. Zhou, E. J. Lavernia, and J. M. Schoenung, "On the evolution of microstructure and defect control in 316L SS components fabricated via directed energy deposition," *Mater. Sci. Engineering: A*, vol. 764, Sep. 2019, Art. no. 138243.
- [44] V. Pandiyan, R. Drissi-Daoudi, S. Shevchik, G. Masinelli, T. Le-Quang, R. Logé, and K. Wasmer, "Deep transfer learning of additive manufacturing mechanisms across materials in metal-based laser powder bed fusion process," *J. Mater. Process. Technol.*, vol. 303, May 2022, Art. no. 117531.
- [45] H. Park, Y. S. Kang, S.-K. Choi, and H. W. Park, "Quality evaluation modeling of a DED-processed metallic deposition based on ResNet-50 with few training data," *J. Intell. Manuf.*, vol. 2024, pp. 1–17, Apr. 2024.
- [46] C. Szegedy, S. Ioffe, V. Vanhoucke, and A. Alemi, "Inception-v4, inception-ResNet and the impact of residual connections on learning," in *Proc. AAAI Conf. Artif. Intell.*, Feb. 2017, vol. 31, no. 1, pp. 4278–4284.
- [47] Y. Yu, J. Huang, L. Wang, and S. Liang, "A 1D-inception-ResNet based global detection model for thin-skinned multifruit spectral quantitative analysis," *Food Control*, vol. 167, Jan. 2025, Art. no. 110823.
- [48] B. Alotaibi and M. Alotaibi, "A hybrid deep ResNet and inception model for hyperspectral image classification," PFG – J. Photogramm., Remote Sens. Geoinf. Sci., vol. 88, no. 6, pp. 463–476, Dec. 2020.
- [49] M. Akbari and R. Kovacevic, "Closed loop control of melt pool width in robotized laser powder–directed energy deposition process," *Int. J. Adv. Manuf. Technol.*, vol. 104, nos. 5–8, pp. 2887–2898, Oct. 2019.
- [50] C. Knaak, L. Masseling, E. Duong, P. Abels, and A. Gillner, "Improving build quality in laser powder bed fusion using high dynamic range imaging and model-based reinforcement learning," *IEEE Access*, vol. 9, pp. 55214–55231, 2021.
- [51] R. R. Selvaraju, M. Cogswell, A. Das, R. Vedantam, D. Parikh, and D. Batra, "Grad-CAM: Visual explanations from deep networks via gradient-based localization," in *Proc. IEEE Int. Conf. Comput. Vis.* (ICCV), Oct. 2017, pp. 618–626.
- [52] J. T. Springenberg, A. Dosovitskiy, T. Brox, and M. Riedmiller, "Striving for simplicity: The all convolutional net," 2014, arXiv:1412.6806.
- [53] D. Smilkov, N. Thorat, B. Kim, F. Viégas, and M. Wattenberg, "Smooth-Grad: Removing noise by adding noise," 2017, arXiv:1706.03825.



CHARLES SNYERS received the B.S. and M.S. degrees in electromechanical engineering from Université Catholique de Louvain, Belgium, in 2014 and 2016, respectively. He is currently pursuing the Ph.D. degree with the Additive Manufacturing Research Group, Vrije Universiteit Brussel, Belgium.

In 2017 and 2018, he was a R&T Engineer at Safran Aero Boosters, Belgium. From January 2019 to December 2019, he was a Graduate

Trainee at European Space Agency, Cologne, Germany, where he researched potential applications of fused deposition modeling to human space flight. In 2020, he joined the Department of Mechanical Engineering, Vrije Universiteit Brussel. His research interests include metal additive manufacturing process optimization and deep learning applied to image processing.



JULIEN ERTVELDT received the degree in industrial engineering (electromechanics) from Erasmus University College Brussels, Belgium, in 2011, the M.Sc. degree in aerospace vehicle design from Cranfield University, U.K., in 2013, and the Ph.D. degree in engineering from Vrije Universiteit Brussels (VUB), Belgium, in 2017, with its work on "Application of Frequency-Domain System Identification to Wind Tunnel Experiments on the Active Aeroelastic Test Bench"

From 2018 to 2023, he was a Research Engineer at the Department of Mechanical Engineering, VUB, on the development of integrated hybrid CNC machining systems combining laser metal deposition, laser ablation, and milling.



KYRIAKOS EFTHYMIADIS received the Ph.D. degree in computer science from the University of York, U.K., in 2014, under the supervision of Dr. Daniel Kudenko. His Ph.D. degree addressed the effects of reward shaping in reinforcement learning under incomplete or underspecified knowledge.

He is currently a Postdoctoral Researcher at Vrije Universiteit Brussel, Belgium. His research interests include deep learning, computer vision,

and reinforcement learning. He is also very interested in applications of deep learning techniques in biology, chemistry, and physics.



JAN HELSEN received the M.Sc. and Ph.D. degrees in electromechanical engineering from Katholieke Universiteit Leuven, Leuven, Belgium, in 2007 and 2012, respectively. His Ph.D. thesis was focused on the dynamic simulation of wind turbine gearboxes.

He is currently a Professor with the Acoustics and Vibrations Research Group, Vrije Universiteit Brussel, Brussel, Belgium. His current research interest includes condition monitoring of rotating systems

• • •